PERGAMON

International Journal of Solids and Structures 37 (2000) 5465–5492

INTERNATIONAL JOURNAL OF SOLIDS and STRUCTURES

www.elsevier.com/locate/ijsolstr

Interaction of an edge dislocation with a thin-film-covered crack

Tong-Yi Zhang*, Cai-Fu Qian[1], Tianhong Wang, Pin Tong

Department of Mechanical Engineering, Hong Kong University of Science and Technology, Clear Water Bay, Kowloon, Hong Kong

Received 4 September 1998; in revised form 27 August 1999

Abstract

The interaction of an edge dislocation with a thin-film-covered crack under mode I and/or mode II loadings is studied in order to investigate the effects of a passive film on stress-corrosion cracking. The passive film is modeled to be an ellipse in which there is a crack. The ellipse is embedded in an infinite medium under remote loadings. Superposition, Cauchy integration, specially constructed functions, and series expansion technique are used to do as much analytical calculation as possible of the stress fields in the film and the substrate. The image force and the shielding effect are calculated and the critical stress intensity factor for dislocation emission from the film-covered crack tip is investigated on the basis of the Rice–Thomson model. The results show that the slip component of the image force of an edge dislocation in the film increases with increasing the ratio of the film shear modulus over the substrate shear modulus, as does the shielding effect of the dislocation on the crack tip. Since the presence of the thin film changes both the image force of the dislocation and the local stress field due to the applied loads, the nominally critical stress intensity factor for dislocation emission is related to the thin film thickness, the properties of the film and the loading conditions. For a given loading mode and crack length, there is a critical value of the film thickness at which the film does not influence the dislocation emission. When the film thickness is smaller than the critical one, a harder thin film makes the dislocation emission easier and a softer film makes the dislocation emission more difficult. The opposite is also true if the film thickness is larger than the critical value for a given crack length. © 2000 Elsevier Science Ltd. All rights reserved.

Keywords: Micro-mechanics; Inclusions; Crack; Dislocations; Stress intensity; Stress-corrosion cracking

---

* Corresponding author: Tel.: +852-2358-7192; fax: +852-2358-1543.
E-mail address: mezhangt@ust.hk (T.-Y. Zhang).

[1] Visiting scholar from the Department of Mechanical Engineering, Beijing University of Chemical Technology, Beijing 100029, People's Republic of China.

PII: S0020-7683(99)00238-3

1. Introduction

Stress-corrosion cracking (SCC), which occurs under the resultant action of mechanical loads and corrosive environments, can cause catastrophic failures of engineering structures and components. Although all SCC failure is macroscopically brittle, localized plastic deformation has been observed at the crack tip, which means that the dislocation activities at the crack tip must be involved during SCC. In order to understand SCC, considerable research has been addressed (e.g. Parkins, 1992; Jones and Ricker, 1992; Sieradzki, 1982; Kaufman and Fink, 1988; Sieradzki and Newman, 1985, 1987; Zhang and Qian, 1996a, 1996b) and many mechanisms have been proposed (Jones and Ricker, 1992; Flanagan et al., 1993; Magnin, 1996), including the corrosion tunnel model, adsorption-enhanced plasticity, film-induced cleavage, adsorption-induced brittle fracture and hydrogen embrittlement. Recently, Magnin (1996) published a book on corrosion-deformation interactions. In this book, he reviewed experimental evidence and associated modeling of corrosion-deformation interactions occurring during SCC.

During SCC, especially in a metal/environment system, a film can be formed. The film may be a passive layer, tarnished film, or a dealloyed layer. The thin film formed is quite different from its substrate in chemical, structural and mechanical properties. Thus, Sieradzki (1982) and Sieradzki and Newman (1985, 1987) proposed a mechanism of film-induced cleavage for SCC based on dislocation-crack interactions. The dislocation emission from a crack tip may become difficult if a thin film with the thickness of several 100 nm is formed around the crack tip owing to an anodic process. Also, a thin ductile film may initiate cleavage if the interface between the film and the substrate is coherent and appropriate mismatch strains exist. The model of film-induced cleavage has successfully described their experimental observations (Sieradzki, 1982; Sieradzki and Newman, 1985, 1987). In order to put the model of film-induced cleavage within a more theoretical context, Zhang and Qian (1996a, 1996b) modeled SCC with a thin-film-covered crack under anti-plane deformation by studying analytically, the interaction between a screw dislocation and the thin-film-covered crack. Their results (Zhang and Qian, 1996a, 1996b) indicate that the crack stress field due to the applied load is enhanced by a harder film or abated by a softer film. If the film thickness is much smaller than the crack length, then the stress intensity factor can be simply expressed as the product of the nominal stress intensity factor and the shear modulus ratio. Both the critical stress intensity factors for the screw dislocation emission from the crack tip and screw dislocation dipole emission from the interface are greatly influenced by the film stiffness and thickness. The advantage of analyzing a film-covered mode III crack lies in the fact that the solution is analytic and given in series (Zhang and Qian, 1996a, 1996b). However, most SCC occurs under mode I loadings. In order to have a better understanding of SCC, the present work, following the previous approach (Zhang and Qian, 1996a, 1996b), studies the effects of thin film formation at a crack tip on fracture under mode I and/or mode II loadings.

From a mechanics point-of-view, the thin-film-covered crack embedded in an infinite medium is also a topic of considerable interest because it is equivalent to a crack in an inclusion. In general, it is very difficult to obtain a closed-form solution for the stress and displacement fields, even in a two-dimensional analysis. Many researches have studied the inclusion problems (Eshelby, 1957; Chen, 1967; Erdogan et al., 1974; Yang and Chou, 1976; Mura, 1982, 1988; Patton and Santare, 1990; Chen, 1995; Dundurs and Mura, 1964; Dundurs and Sedeckyj, 1965; Gong, 1994; Qaissaunee and Santare, 1995; Santare, 1995; Santare and Keer, 1986; Stagni and Lizzio, 1983; Tong and Zhang, 1996; Warren, 1983; Yen et al., 1995; Wu and Chen, 1990; Anlas and Santare, 1993; Yen and Hwu, 1994; Honein et al., 1994). Interested readers may first consult with the book and paper by Mura (1982, 1988), which are overviews of the methodologies and solutions to inclusion problems. Here, we briefly introduce the works that are more relevant to the present topic. Wu and Chen (1990) studied a crack in confocal elliptic inhomogeneity embedded in an infinite medium under anti-plane and/or in-plane loadings. They found that the solution for the anti-plane problem is exact and can serve as a quantitative indication of the behaviors of the solutions to the in-plane problems that cannot be solved exactly. As mentioned above, the thin-film-covered crack has been studied under mode III loadings and those results will be used here for comparison. Anlas and Santare (1993) studied the problem of an arbitrarily oriented crack inside an elliptical inclusion. They used the complex potentials for an edge dislocation inside an elastic elliptical inclusion (Qaissaunee, 1992) as the Green's function and expressed the solution in terms of singular integral equations that have to be solved numerically.

Taking advantage of the above mentioned work, the present work studies the interaction of an edge dislocation with a thin-film-covered crack. For simplicity, the whole system studied here is assumed to be initially stress-free. Actually, residual stresses may be induced during SCC, which will be considered for future research. Muskhelishvili's complex potentials (1954), superposition, analytic continuation, Cauchy integration and Laurent series are deliberately combined to calculate the stress fields in both the film and the substrate. The new methodology is able to produce the best possible analytical solutions. Consequently, the effects of the film stiffness and thickness on the crack tip stress field due to applied loads, on the image force, on the shielding effect, and on the dislocation emission from the film-covered crack tip are studied in order to explore the role of the thin film formation during SCC.

2. Analysis

In order to model a crack covered by a thin film, we assume that the film has an elliptical shape of $x_1^2/a^2+x_2^2/h^2=1$. Inside the film, there is a crack extending from $-c$ to c along the x_1 axis with $c^2=a^2-h^2$. The crack and the film are embedded in an infinite medium under remote loadings, as shown in Fig. 1(a). The conformal mapping function

$$z=\omega(\zeta)=R\left(\zeta+\frac{m}{\zeta}\right), \tag{1}$$

where $z=x_1+ix_2$, $\zeta=\eta+i\xi$, $R=(a+h)/2$ and $m=(a-h)/(a+h)$, maps the ellipse in the z-plane into a unit circle in the ζ-plane and the crack $(-c, c)$ in the z-plane into a circle with a radius of $\sqrt{m}$ in the ζ-plane, as shown in Fig. 1(b). The inverse mapping function of (1) is

$$\zeta=\frac{z+\sqrt{z^2-c^2}}{2R} \tag{2}$$

Thus, the problem in the z-plane can be solved in the ζ-plane using the conformal mapping functions.

For in-plane strain, the stress and displacement fields can be expressed by two complex potentials

$$\sigma_{11}+\sigma_{22}=2\left[\phi'(z)+\overline{\phi'(z)}\right],$$

$$\sigma_{22}-\sigma_{11}+2i\sigma_{12}=2\left[\bar{z}\phi''(z)+\psi'(z)\right],$$

$$u(z)=u_1+iu_2=\frac{1}{2\mu}\left[\kappa\phi(z)-z\overline{\phi'(z)}-\overline{\psi(z)}\right], \tag{3}$$

where the prime denotes the differentiation with respect to z, the overbar denotes complex conjugate, $\kappa=3-4\nu$, and μ and ν are, respectively, the shear modulus and Poisson ratio of the material.

The traction-free boundary condition along the crack faces requires

$$\phi^*(t) + \frac{\omega(t)}{\overline{\omega'(t)}}\overline{\phi^{*\prime}(t)} + \overline{\psi^*(t)} = 0 \quad \text{at } t = \sqrt{m}e^{i\theta}, \tag{4}$$

where the superscript '*' denotes the film. From the boundary conditions of continuity of displacement and traction along the interface, i.e., along the unit circle, the complex potentials for the substrate can be expressed in terms of the complex potentials for the thin film.

$$\phi(t) = a_1\phi^*(t) + a_2\left[\frac{t^2+m}{t(1-mt^2)}\overline{\phi^{*\prime}(t)} + \overline{\psi^*(t)}\right] \quad \text{at t} = \text{e}^{i\theta} \tag{5}$$

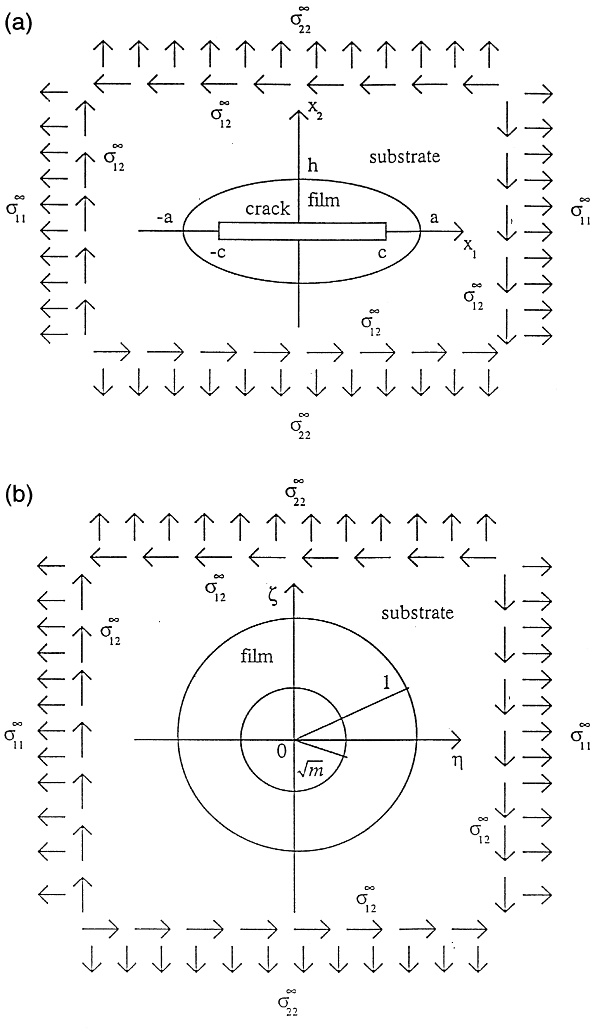

Fig. 1. (a) Schematic illustration of a thin-film-covered crack under remote applied loads in the z-plane. (b) Mapping the thin-film-covered crack into a circular ring in the ζ plane.

$$\frac{t^2+m}{t(1-mt^2)}\overline{\phi'(t)}+\overline{\psi(t)}=a_3\phi^*(t)+a_4\left[\frac{t^2+m}{t(1-mt^2)}\overline{\phi^{*\prime}(t)}+\overline{\psi^*(t)}\right],\quad \text{at } \mathrm{t}=\mathrm{e}^{i\theta} \tag{6}$$

where

$$\Gamma=\mu^*/\mu,\quad a_1=\frac{\kappa^*+\Gamma}{\Gamma(\kappa+1)},\quad a_2=\frac{\Gamma-1}{\Gamma(\kappa+1)},\quad a_3=\frac{\Gamma\kappa-\kappa^*}{\Gamma(\kappa+1)},\quad \text{and}\quad a_4=\frac{\Gamma\kappa+1}{\Gamma(\kappa+1)}. \tag{7}$$

The detailed derivations of the stress fields produced by applied remote loads and an edge dislocation within the film are respectively given in Appendices A and B.

3. Results and discussion

3.1. The stress fields due to applied remote loads

Appendix A describes the detailed analysis of the stress fields induced by applied remote loads including σ_{11}^{∞}, σ_{12}^{∞} and σ_{22}^{∞}. However, the following discussion will not consider the remote load of σ_{11}^{∞} for simplicity, i.e., $\sigma_{11}^{\infty}=0$ is implicitly adopted as follows. In this study, the length is scaled in units of the magnitude of the Burgers vector $b=|\mathbf{b}|=|b_1+ib_2|=\sqrt{b_1^2+b_2^2}$, and b_1 and b_2 are, respectively, the components of the Burgers vector along the x_1 and x_2 axes. Fig. 2(a) and (b) show the normalized stresses in front of the crack tip as a function of the shear modulus ratio, Γ, wherein the crack length c = 19,900b, the film thickness a–c along the x_1 axis is 100b, the locations, at which the stresses are calculated, are 50b in the film and 150b in the substrate from the crack tip, respectively. As can be seen in Fig. 2(a), the normalized stresses increase monotonically from 8.5, 9.0 and 7.5 to 18.0, 18.0 and 25.0, respectively, for $\sigma_{11}/\sigma_{22}^{\infty}$, $\sigma_{22}/\sigma_{22}^{\infty}$ and $\sigma_{12}/\sigma_{12}^{\infty}$ when the shear modulus ratio increases from 0.5 to 2.0. This phenomena for the inplane deformation is similar to that for the anti-plane deformation (Zhang and Qian, 1996a). A softer film reduces the stress field in the film, while a harder film enhances it. The stress behavior in the substrate differs from that in the film. Fig. 2(b) shows that when the shear modulus ratio increases from 0.5 to 2.0, the normalized stresses $\sigma_{11}/\sigma_{22}^{\infty}$ and $\sigma_{12}/\sigma_{12}^{\infty}$ increase monotonically from 6.0 and 6.2 to 8 and 10.5, respectively, while $\sigma_{22}/\sigma_{22}^{\infty}$ decreases monotonically from 10.2 to 6.2. The reason that $\sigma_{11}/\sigma_{22}^{\infty}$ and $\sigma_{12}/\sigma_{12}^{\infty}$ behave in the substrate in the same way as that in the film lies in the fact that these stress components are continuous at the interface along the x_1 axis. The stress component σ_{22} jumps when crossing the interface, as shown in Fig. 3, where the σ_{22} distribution along the x_1 axis is given for two different ratios of shear moduli. When crossing the interface from the film to the substrate, the normalized stress $\sigma_{22}/\sigma_{22}^{\infty}$ jumps up from 9 to 14 for a softer film with $\Gamma=0.5$, while it jumps down from 8 to 7 for a harder film with $\Gamma=2$. Clearly, σ_{22} is discontinuous across the interface and the magnitude of the jump depends on the ratio of shear moduli. The discontinuity of the stress fields across the interface between the film and the substrate could be an important influence factor on SCC in a way of affecting, for example, the dislocation activities in front of the crack tip. Figs. 4(a)–(d) illustrate the effects of the Poisson ratio of the thin film on the stress fields in both film and substrate for $\Gamma=0.5$ and 2, where the Poisson ratio of the substrate is taken to be 0.3. For the stress field in the film, as shown in Fig. 4(a) and (b), when the Poisson ratio of the film increases from 0.25 to 0.45, the normalized stresses $\sigma_{11}/\sigma_{22}^{\infty}$, $\sigma_{22}/\sigma_{22}^{\infty}$ and $\sigma_{12}/\sigma_{12}^{\infty}$ increase, respectively, from 7.8, 8.7 and 7.2 to 11.4, 12.8 and 9.2 for $\Gamma=0.5$, while increase, respectively, from 17.7, 17.7 and 23.6 to 21.6, 20.8 and 29.7 for $\Gamma=2$. Therefore, a large Poisson ratio of the film enhances all stress components in the film, regardless of the ratio of shear moduli. Fig. 4(c) and (d) demonstrate the stress field in the substrate as a function of the Poisson ratio of the film. For $\Gamma=0.5$, the normalized stresses $\sigma_{11}/\sigma_{22}^{\infty}$ and $\sigma_{12}/\sigma_{12}^{\infty}$ increase, respectively, from 5.7 and 6.1 to 7.2 and 7.0, while $\sigma_{22}/\sigma_{22}^{\infty}$ decreases from 10.5 to 8.7,

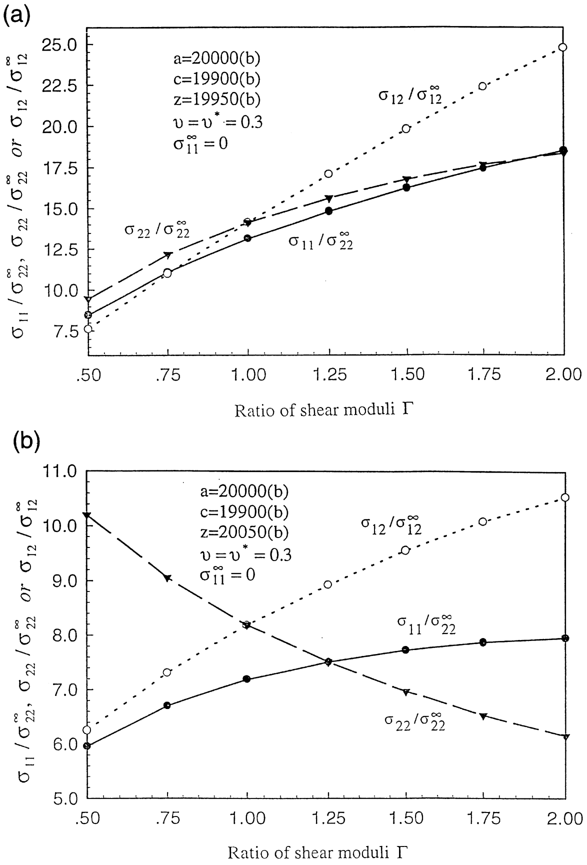

Fig. 2. (a) The variation of the normalized stresses in the film, at a point 50*b* away from the crack tip along the x_1, axis, with the shear modulus ratio Γ. (b) The variation of the normalized stresses in the substrate, at a point 50*b* away from the interface along the x_1, axis, with the shear modulus ratio Γ.

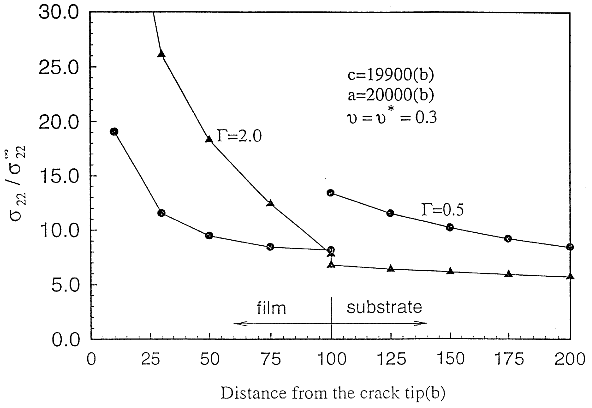

Fig. 3. Distribution of the normalized stress $\sigma_{22}/\sigma_{22}^{\infty}$ in front of the crack tip along the x_1 axis for $\Gamma = 0.5$ and 2.

as the Poisson ratio of the film increases from 0.25 to 0.45. Similar behaviors of the stress components are found for $\Gamma = 2$. When the Poisson ratio of the film increases from 0.25 to 0.45, the normalized stresses $\sigma_{11}/\sigma_{22}^{\infty}$ and $\sigma_{12}/\sigma_{12}^{\infty}$ increase respectively, from 7.8 and 10.2 to 8.6 and 11.6, while $\sigma_{22}/\sigma_{22}^{\infty}$ decreases from 6.5 to 5.0. These facts indicate that a large Poisson ratio of the film leads to high stresses $\sigma_{11}/\sigma_{22}^{\infty}$ and $\sigma_{12}/\sigma_{12}^{\infty}$ and a low stress $\sigma_{22}/\sigma_{22}^{\infty}$ in the substrate, in spite of the ratio of shear moduli.

The stress intensity factors at the right crack tip are defined as

$$K_{\mathrm{I}} + iK_{\mathrm{II}} = \lim_{z \to c} \sqrt{2\pi(z-c)}(\sigma_{22} + i\sigma_{12}). \tag{8}$$

Substituting σ_{22} and σ_{12} into Eq. (8) and completing the limit lead to

$$K_{\mathrm{I}} + iK_{\mathrm{II}} = \sqrt{\pi c}\left(c_1 + \overline{c_1} + c_2 + \sum_{n=-\infty}^{\infty} \frac{C_n + 2\overline{C_n}}{2R} nm^{\frac{n-1}{2}}\right), \tag{9}$$

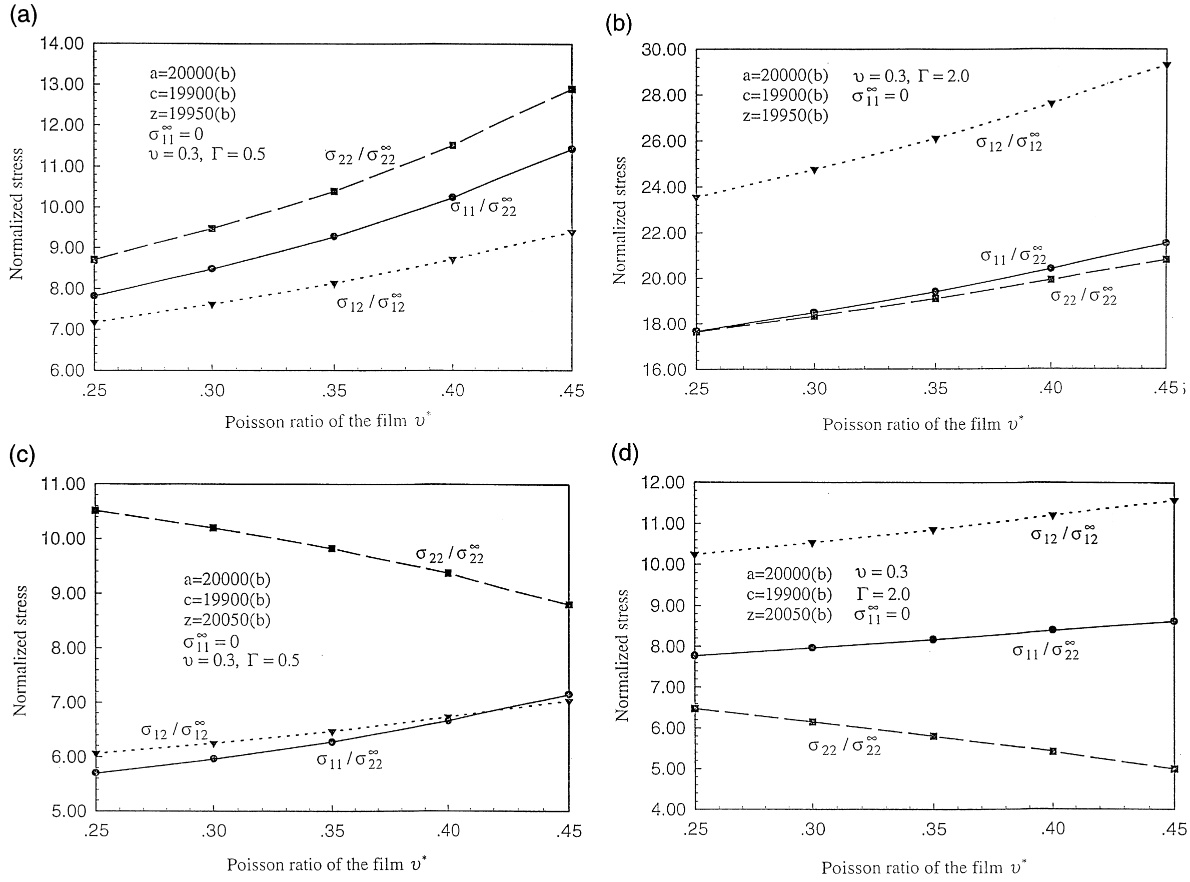

Fig. 4. (a) The variation of the normalized stresses in the film, at a point 50*b* away from the crack tip along the x_1 axis, with the Poisson ratio of the film for $\Gamma = 0.5$. (b) The variation of the normalized stresses in the film, at a point 50*b* away from the crack tip along the x_1 axis, with the Poisson ratio of the film for $\Gamma = 2$. (c) The variation of the normalized stresses in the substrate, at a point 50*b* away from the interface along the x_1 axis, with the Poisson ratio of the film for $\Gamma = 0.5$. (d) The variation of the normalized stresses in the substrate, at a point 50*b* away from the interface along the x_1 axis, with the Poisson ratio of the film for $\Gamma = 2$.

where c_1, c_2 and C_n are parameters evaluated in Appendix A, c_1 and c_2 are given in Eq. (A13) and C_n has to be numerically calculated from Eqs. (A18) and (A19). Fig. 5 shows the normalized stress intensity factor as a function of the film thickness *a–c* for $\Gamma = 0.5$ and 2, where,

$$K_{\mathrm{I}}^{0} = \sqrt{\pi c}\sigma_{22}^{\infty}, \tag{10}$$

$$K_{\mathrm{II}}^{0} = \sqrt{\pi c}\sigma_{12}^{\infty} \tag{11}$$

are the nominal stress intensity factors without any film. As in the analytically studied case for the mode III crack (Zhang and Qian, 1996a), the normalized stress intensity factors decrease with increasing the film thickness if the film is harder than the substrate, as shown in Fig. 5 for $\Gamma = 2$. However, if the film is softer than the substrate, the normalized stress intensity factors increase with increasing the film thickness, as also shown in Fig. 5 for $\Gamma = 0.5$. It is also seen that the effect of the film thickness on the normalized stress intensity factors is stronger for mode II loading than that for mode I loading. $K_{\mathrm{I}}/K_{\mathrm{I}}^{0}$ slightly increases from 1.40 to 1.42 for $\Gamma = 2$ and decreases from 0.64 to 0.63 for $\Gamma = 0.5$, as the film thickness decreases from 100 to 5*b* This means that $K_{\mathrm{I}}/K_{\mathrm{I}}^{0}$ is insensitive to the film thickness in the range of $a–c = 5–100b$. On the other hand, when the film thickness decreases from 100 to 5*b*, $K_{\mathrm{II}}/K_{\mathrm{II}}^{0}$ increases from 1.78 to 2.0 for $\Gamma = 2$ and decreases from 0.53 to 0.50 for $\Gamma = 0.5$. The behavior of $K_{\mathrm{II}}/K_{\mathrm{II}}^{0}$ is similar to that of $K_{\mathrm{III}}/K_{\mathrm{III}}^{0}$ i.e., the stress intensity factor is proportional to the ratio of shear moduli when the film thickness is very small. Fig. 6 shows the normalized stress intensity factors as functions of the ratio of shear moduli, where the film thickness remains at 100*b*. When the ratio of shear moduli increases from 0.5 to 2, $K_{\mathrm{I}}/K_{\mathrm{I}}^{0}$ and $K_{\mathrm{II}}/K_{\mathrm{II}}^{0}$ increase from 0.64 and 0.54 to 1.40 and 1.78, respectively. Clearly, a large Γ corresponds to high normalized stress intensity factors and this influence on K_{II} is also stronger than that on K_{I}. Fig. 7(a) and (b) are plots of the normalized stress intensity factor as a function of the Poisson ratio of the film, respectively, for $\Gamma = 0.5$ and 2, where the Poisson ratio of the substrate is taken to be 0.3 or 0.45. Similar to the effects of the Poisson ratio of the film on the stress field in the film, a large Poisson ratio of the film yields high stress intensity factors regardless of the ratio of shear moduli, as shown in Fig. 7(a) and (b).

3.2. Image force and shielding effects of an edge dislocation in the film

Appendix B shows the detailed derivation of the complex potentials produced by an edge dislocation

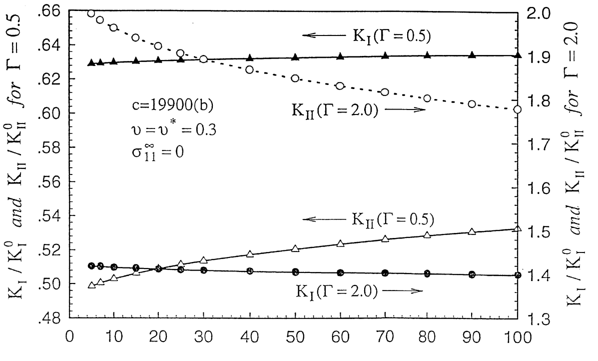

Fig. 5. The normalized stress intensity factors as a function of film thickness for $\Gamma = 0.5$ and 2.

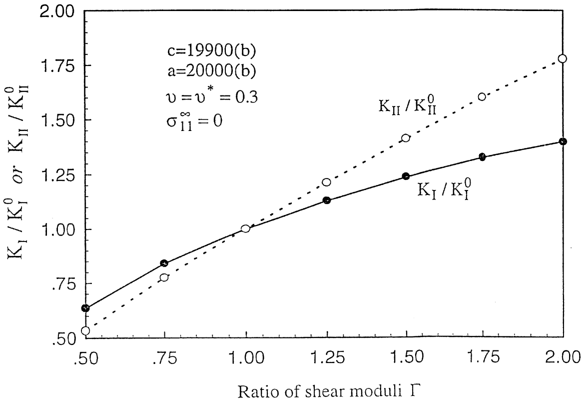

Fig. 6. The normalized stress intensity factors as a function of the shear modulus ratio Γ.

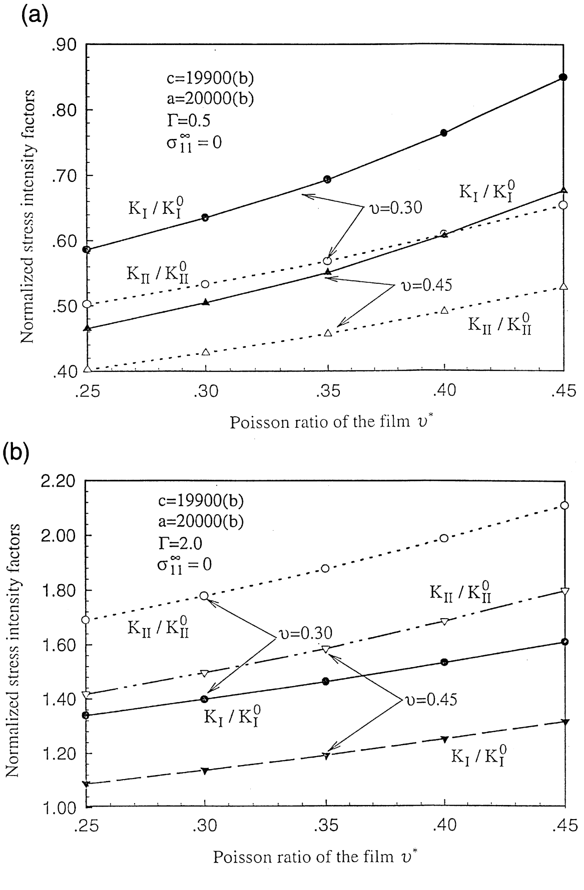

Fig. 7. The normalized stress intensity factors as a function of the Poisson ratio of the film, (a) for $\Gamma = 0.5$ and (b) for $\Gamma = 2$.

located inside the film. The stress field near a finite length crack produced by a dislocation is related to dislocation sources (Zhang and Li, 1991). The present work, as stated in Appendix B, considers only dislocations emitted from the crack. Using Eq. (3), the stress fields are calculated by these complex potentials derived in Appendix B. Fig. 8 shows the stress distribution of σ_{12} along the x_1 axis for $\Gamma = 2$, 1 and 0.5, where the crack length $c = 19{,}900b$, the film thickness a–$c = 100b$, and the dislocation is located 25b away from the crack tip. It is seen that higher the ratio of the shear moduli, i.e., higher the stiffness of the film, the higher the stress field within the film.

The force exerted on a unit length of dislocation is given by the Peach–Koehler formula

$$F = F_1 + iF_2 = (\sigma_{12}b_1 + \sigma_{22}b_2) - i(\sigma_{11}b_1 + \sigma_{12}b_2). \tag{12}$$

The image force of the dislocation can be calculated from the stress field due to its images by letting $z = z_d(\zeta = \zeta_d)$. The image force exerted on a dislocation usually has slip and climb components. The present work studies only the slip component of the image force. For convenience, we translate the origin to the right crack tip. The dislocation location is then expressed as $z_d = re^{i\theta} + c$, where r is the distance between the right crack tip and the dislocation and θ is the polar angle. The present work assumes also that the Burgers vector of the dislocation has the same polar angle as the slip plane. As an example, Fig. 9 demonstrates the slip image force as a function of r for different slip planes under a given crack length of $c = 19{,}900b$, a film thickness of a–c = 100b and a ratio of shear moduli $\Gamma = 0.5$. It is seen that the inclination of slip planes has a slight influence on the slip image force especially when the dislocation is near the crack tip. This is because the slip image force of a dislocation is independent of the inclination of slip planes for a semi-infinite length crack without being covered by any film (Rice and Thomson, 1974; Asaro, 1975). As discussed by Zhang and Qian (1996a), both the crack and the interface produce image forces on a dislocation in the film. When the dislocation is very close to the crack tip, the image force due to the crack dominates, while the interface becomes the major contributor to the image force when the dislocation is far from the crack tip and close to the interface. In the latter case, the slip image force depends on the angle of the slip plane, as shown in Fig. 9, and the larger the angle, the smaller the slip image force in magnitude. Note that the minus sign indicates the image force towards to the crack tip, and thereafter "a large image force" will be used to indicate that the image force has a large value of magnitude. Under a pure mode I loading, the maximum shear stress occurs at the slip plane with a polar angle of 70°. This implies that it is relatively easy for the crack to emit an edge dislocation along the 70°-slip plane. Therefore, the 70°-slip plane will be discussed more in the

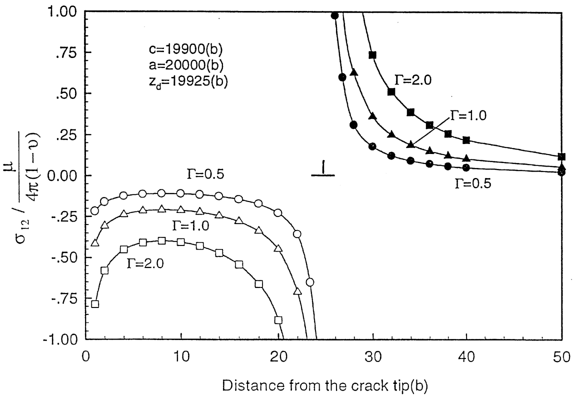

Fig. 8. Stress distribution along the crack plane for three ratios of shear moduli, where the edge dislocation is located 25b in front of the crack tip in the crack plane.

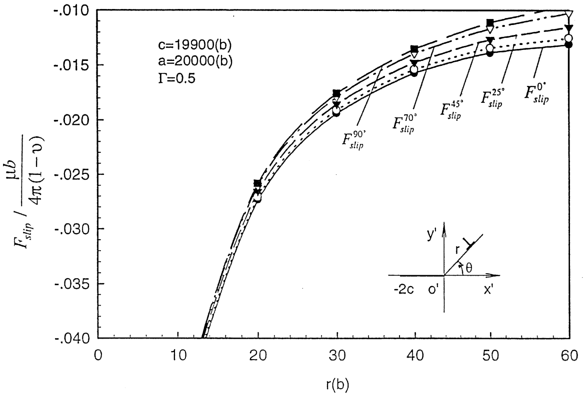

Fig. 9. The slip image force of an edge dislocation in different slip planes as a function of the distance from the dislocation to the crack tip.

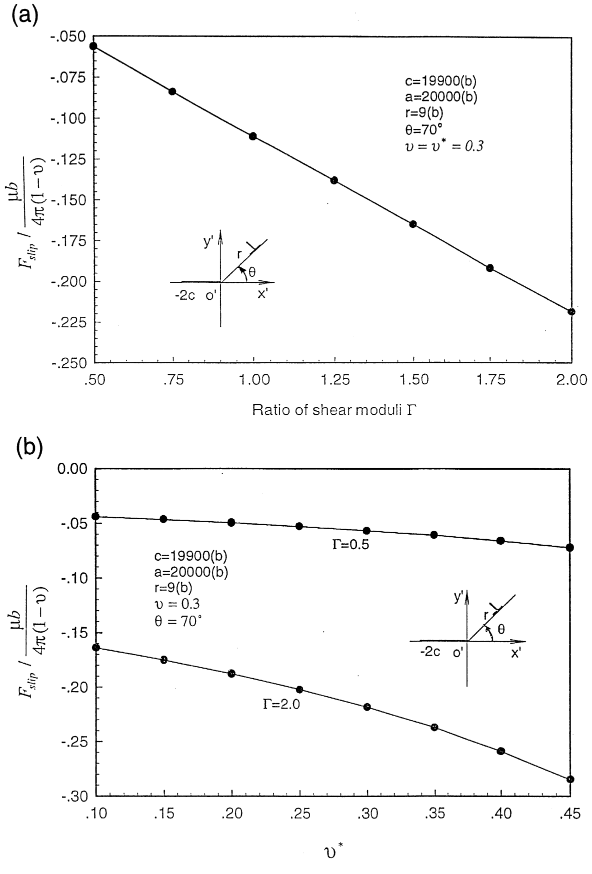

Fig. 10. The slip image force of an edge dislocation in the 70° slip plane as a function of: (a) the shear modulus ratio Γ and (b) the Poisson ratio of the film.

following. Fig. 10(a) illustrates the slip image force as a function of the ratio of shear moduli for the 70°-slip plane, where the dislocation is located $9b$ away from the right crack tip. The slip image force is directly proportional to the ratio of shear moduli Γ, as shown in Fig. 10(a), indicating that a hard film corresponds to a high image force. Fig. 10(b) demonstrates the variation of the slip image force with the Poisson ratio of the film for $\Gamma = 0.5$ and 2, where the Poisson ratio of the substrate is taken to be 0.3. Regardless of the value of the shear modulus ratio, the slip image force monotonically increases with increasing the Poisson ratio of the film.

Similar to applied remote loads, an edge dislocation also produces a stress singularity at each crack tip. Using the stress field produced by the edge dislocation and the definition of stress intensity factors of Eq. (11), we calculate the stress intensity factors at the right crack tip induced by the edge dislocation and express them in Eq. (B18) in Appendix B. Fig. 11(a) and (b) respectively show the mode I and mode II stress intensity factors as a function of r for different slip planes where $c = 19{,}900b$, a–c $= 100b$ and $\Gamma = 0.5$. Unlike the slip image force plotted in Fig. 9, the stress intensity factors vary considerably with the slip plane because the Burgers vector of the dislocation changes from one slip plane to another. The dislocation on the 70°- slip plane produces the largest shielding from mode I loading and the smallest shielding from mode II loading, while the shielding effect of the dislocation on the 0°-slip plane is the smallest from mode I loading and the largest from mode II loading. These results

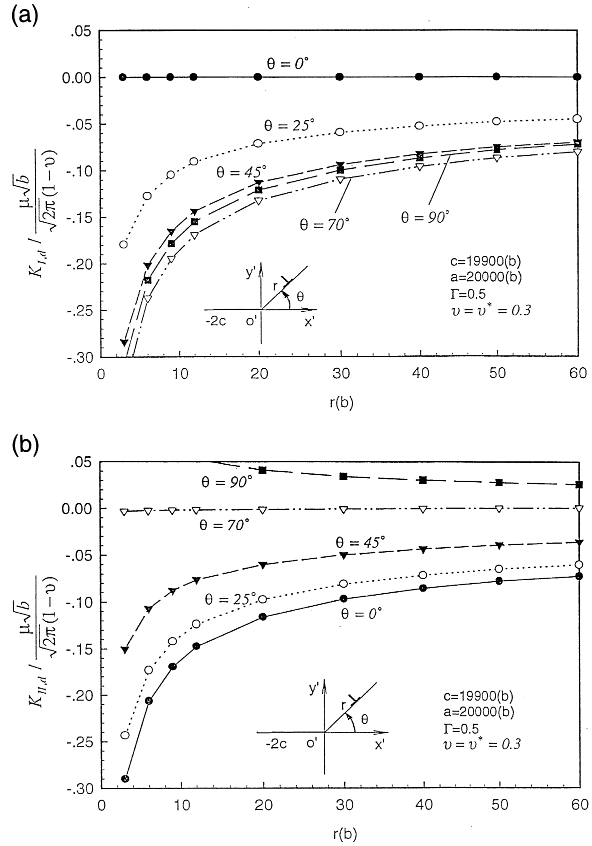

Fig. 11. The stress intensity factor induced by an edge dislocation in different slip planes as a function of the distance from the dislocation to the crack tip. (a) $K_{\mathrm{I,\,d}}$ and (b) $K_{\mathrm{II,\,d}}$.

are consistent with the case for a dislocation emitted from a crack tip in a homogeneous medium (Zhang and Li, 1991; Qian and Li, 1996a, 1996b). The influences of the shear modulus ratio and the Poisson ratio on the dislocation shielding are similar to those on the slip image force of the dislocation. The stress intensity factors produced by the dislocation are proportional to the ratio of shear moduli Γ, as shown in Fig. 12(a), and increase monotonically with increasing the Poisson ratio of the film (Fig. 12(b)).

3.3. Dislocation emission from the crack tip

In order to study how a hard or soft passive film can influence dislocation emission from the crack tip, we calculate the critical stress intensity factor for an edge dislocation emission from the crack tip. The critical stress intensity factor in the two-dimensional Rice–Thomson model is calculated from the balance between the driving force and the image force at a certain distance from the crack tip (Rice and Thomson, 1974; Lin and Thomson, 1986). This distance is usually taken to be the size of the dislocation core cut-off, r_0. The algebraic equation to determine the critical stress intensity factor for dislocation emission is then given by

$$F^{\theta}_{\text{crack}}(r_0) + F^{\theta}_{\text{slip}}(r_0) = 0, \tag{13}$$

where $F^{\theta}_{\text{slip}}(r_0)$ denotes the slip image force and $F^{\theta}_{Crack}(r_0)$ is the slip driving force that can be expressed

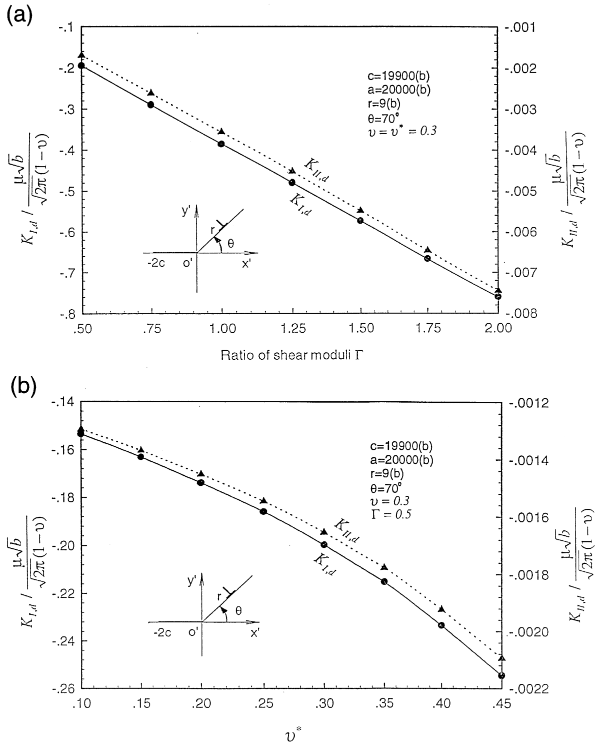

Fig. 12. The stress intensity factors induced by an edge dislocation in the 70° slip plane as a function of: (a) the shear modulus ratio Γ and (b) the Poisson ratio of the film.

in terms of the mode I and mode II intensity factors. Note that both the slip image force and the slip driving force are related to the polar angle. In this study, we discuss two special cases. A pure mode II loading drives the dislocation emission along the crack plane ($\theta = 0°$) and a pure mode I loading may emit dislocation along the 70°-slip plane. The two slip planes are the most favorable planes in studying dislocation emission from a crack tip in an isotropically homogeneous material (Zhang and Li, 1991; Qian and Li, 1996a, 1996b). Thus, the critical mode II or mode I stress intensity factor for dislocation emission can be explicitly written as

$$K_{\mathrm{II,\,e}} = -\frac{\sqrt{2\pi r_0}}{b}\Theta(\theta = 0°)F_{\mathrm{slip}}^{\theta=0°}(r_0), \quad \text{for mode II emission,} \tag{14a}$$

$$K_{\mathrm{I,\,e}} = -\frac{\sqrt{2\pi r_0}}{b}\Theta(\theta = 70°)F_{\mathrm{slip}}^{\theta=70°}(r_0), \quad \text{for mode I emission,} \tag{14b}$$

where Θ is a function of θ and becomes unity for $\theta = 0°$. Since the thin-film may change the stress intensity factors, it is convenient to convert the critical stress intensity factors calculated by Eqs. (14a) and (14b) into the nominal ones:

$$K_{\mathrm{II,\,e}}^{0} = -\frac{i2\sigma_{12}^{\infty}\sqrt{2\pi r_0}F_{\mathrm{slip}}^{\theta=0°}(r_0)}{b\left(c_2 - \overline{c_2} + \sum_{n=-\infty}^{\infty}\frac{\overline{C_n} - C_n}{2R}nm^{\frac{n-1}{2}}\right)}, \quad \text{for mode II emission,} \tag{15a}$$

$$K_{\mathrm{I,\,e}}^{0} = -\frac{2\sigma_{22}^{\infty}\sqrt{2\pi r_0}\Theta(\theta = 70°)F_{\mathrm{slip}}^{\theta=70°}(r_0)}{b\left(2c_1 + 2\overline{c_1} + c_2 + \overline{c_2} + \sum_{n=-\infty}^{\infty}\frac{3\overline{C_n} + 3C_n}{2R}nm^{\frac{n-1}{2}}\right)}, \quad \text{for mode I emission,} \tag{15b}$$

It should be pointed out that in calculating these parameters of c_1, c_2 and C_n to evaluate the nominally critical stress intensity factors for dislocation emission, σ_{22}^{∞} should be taken as zero for the mode II emission and as should σ_{12}^{∞} for the mode I emission. Furthermore, the cut-off of dislocation core in the present study is taken to be $r_0 = 1\,b$.

Fig. 13(a) and (b) show the critical stress intensity factors, $K_{\mathrm{I,\,e}}$ and $K_{\mathrm{II,\,e}}$, respectively, for dislocation emission under mode I and mode II loadings, as functions of the film thickness, while Fig. 14(a) and (b) indicate the corresponding nominal factors. Two crack lengths, $c = 1000b$ and $c = 1{,}000{,}000b$, and two ratios of shear moduli, $\Gamma = 2$ and 0.5, are employed in plotting Figs. 13(a) and 14(a). As can be seen in Figs. 13(a) and 14(a), all the critical stress intensity factors and the nominal ones increase (or decrease) with increasing the film thickness for $\Gamma = 2$ (or $\Gamma = 0.5$) and behave the same for both mode I and mode II emission. This phenomenon was also found for crew dislocation emission from a thin-film-covered mode III crack (Zhang and Qian, 1996a). Fig. 13(a) and (b) show that the two crack lengths, $c = 1000b$ and $c = 1{,}000{,}000b$, yield almost the same critical stress intensity factors in terms of the elastic constants of the substrate, i.e., in units of $\mu\sqrt{b}/[\sqrt{2\pi}(1-\nu)]$, when the film thickness is larger than $10b$ This means that the critical stress intensity factors are insensitive to the crack length when the film thickness is larger than $10b$. If the film thickness is smaller than $10b$, however, the critical stress intensity factors vary with the crack length, as shown in Fig. 13(a) and (b). It is the nominal stress intensity factor that is measurable, therefore, focus will be put on the nominally critical stress intensity factors for dislocation emission.

Fig. 14(a) and (b) illustrate that the nominally critical stress intensity factors increase with the film thickness for $\Gamma = 2$, while decreasing with the film thickness for $\Gamma = 0.5$. The variation of the nominally critical stress intensity factors with the film thickness is greatly affected by the crack length. For $\Gamma = 2$, the nominally critical stress intensity factors for either mode I or mode II emission are higher for the short crack than those for the long crack, and the opposite is also true for $\Gamma = 0.5$. For both mode I and mode II emission, the nominally critical stress intensity factors are, respectively, larger (or smaller) than those in a homogeneous medium film for $\Gamma = 2$ (or $\Gamma = 0.5$) when the film is thicker than a critical value of about $3b$ for $c = 1{,}000{,}000b$ in Fig. 14(a), or of about $5b$ for $c = 1000b$ in Fig. 14(b). The results indicate that a harder film will make the dislocation emission more difficult, while a softer film will promote dislocation emission, if the film thickness is larger than the critical value. On the other hand, a harder film will facilitate dislocation emission and a softer film will retard it, if the film thickness is smaller than the critical thickness. This critical film thickness depends on the loading mode and the crack length. A long crack yields a large critical film thickness. For example, the critical thickness for the mode II loading is about $5b$ for the crack length $c = 1000b$, while it is over $40b$ for $c = 1{,}000{,}000b$, as shown in Fig. 14(b). For a given crack length, e.g. $c = 1{,}000{,}000b$, the critical thickness for the mode I loading is about $3b$, much smaller than that of over $40b$ for the mode II loading, as indicated in Fig. 14(a) and (b). If the crack is short, e.g. $c = 1000b$, the critical film thickness must be smaller than $2b$ for the mode I loading. Since the dislocation core is taken to be $1b$ in

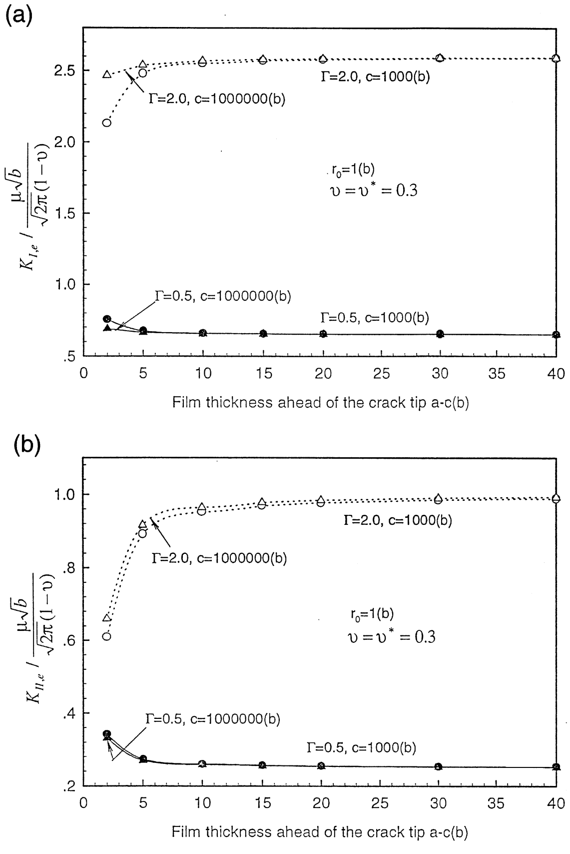

Fig. 13. The critical stress intensity factors for an edge dislocation emission from the thin-film-covered crack tip as a function of the film thickness. (a) For mode I emission and (b) for mode II emission.

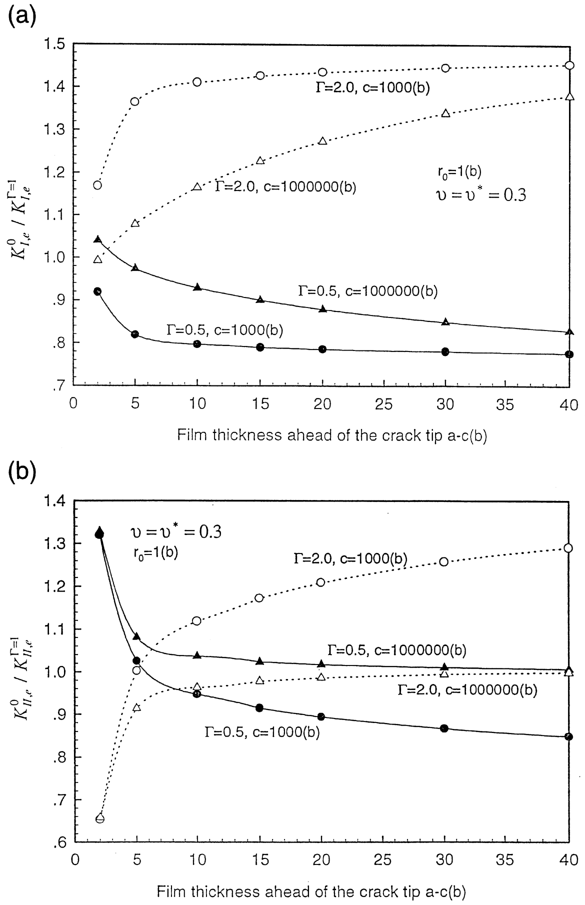

Fig. 14. The nominally critical stress intensity factors for an edge dislocation emission fromthe thin-film-covered crack tip as a function of the film thickness, corresponding the results in Figs. 13 and 14(a) for mode I emission and Fig. 14(b) for mode II emission.

the present study, it will be very difficult and meaningless to conduct the numerical calculation if a film thickness is smaller than 2*b*. Therefore, the critical film thickness cannot be explicitly illustrated in Fig. 14(a). However, the analytical solution is available for a pure mode III load (Zhang and Qian, 1996a), we have explored the critical thickness for the mode III emission in Appendix C. The results show that only when the ratio of the film thickness over the crack length is smaller than 10^{-5}, can the stress intensity factor be approximately expressed as the product of the ratio of moduli and the nominal stress intensity factor within 5% accuracy (see Appendix C). Furthermore, if one uses the approximated stress intensity factor in calculating the nominally critical stress intensity factor for dislocation emission, one will find that a harder film makes the dislocation emission easier and a softer film makes it difficult regardless of the film thickness.[2] The critical film thickness stems from the fact that the exact stress

---

[2] Fig. 7 in Zhang and Qian's work (Zhang and Qian, 1996a) was plotted using the approximated stress intensity factor.

intensity factor decreases (or increases) with increasing the film thickness for a ratio of shear moduli being larger (or smaller) than unity.

Fig. 15(a) and (b) illustrate the critical stress intensity factors and the nominal factors for dislocation emission, under the mode I or mode II loading, as functions of the ratio of shear moduli. Two film thicknesses, $a–c = 5b$ and $10b$, are used in plotting Fig. 15(a) and (b). All the critical stress intensity factors for both film thicknesses increase with increasing the ratio of shear moduli, as shown in Fig. 15(a). Since both the film thicknesses are larger than the critical film thickness for the mode I emission, as expected, the nominally critical stress intensity factors are enhanced by the ratio of shear moduli for both the film thicknesses. However, $a–c = 5b$ is slightly smaller than, and $a–c = 10b$ is larger than, the critical film thickness for the mode II emission. Fig. 15(b) shows that the nominally critical stress intensity factors increase with increasing the ratio of shear moduli if the film thickness is larger than the critical one. The opposite is also true. If the film thickness is smaller than the critical one, the nominally critical stress intensity factors decrease with increasing the ratio of shear moduli.

Fig. 16(a) and (b) show the critical stress intensity factors and the nominal ones for dislocation emission under the mode I or mode II loading as functions of the Poisson ratio of the film, where the Poisson ratio of the substrate is taken to be 0.3. Again, the two film thicknesses, $a–c = 5b$ and $10b$ are

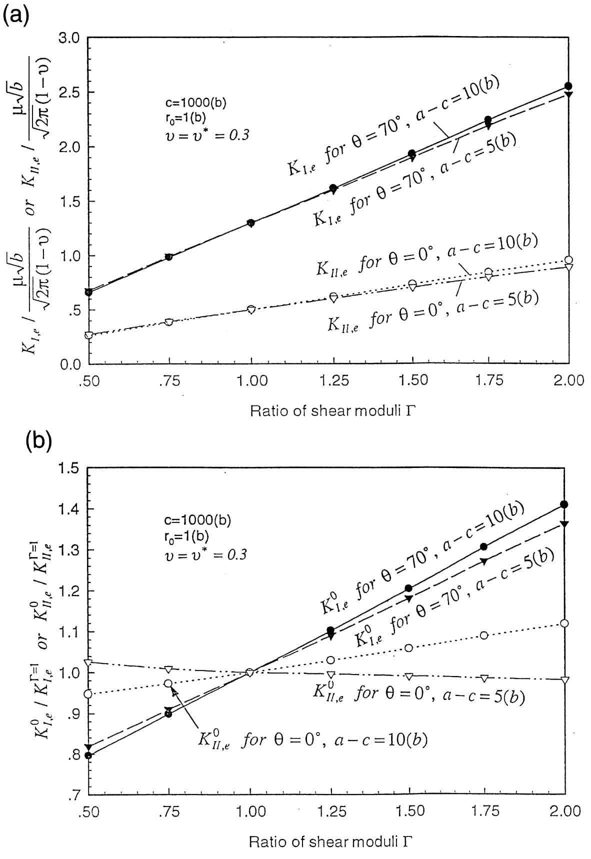

Fig. 15. (a) The critical stress intensity factors for an edge dislocation emission from the thin-film-covered crack tip as a function of the shear modulus ratio Γ. (b) The nominally critical stress intensity factors for an edge dislocation emission from the thin-film-covered crack tip as a function of the shear modulus ratio Γ.

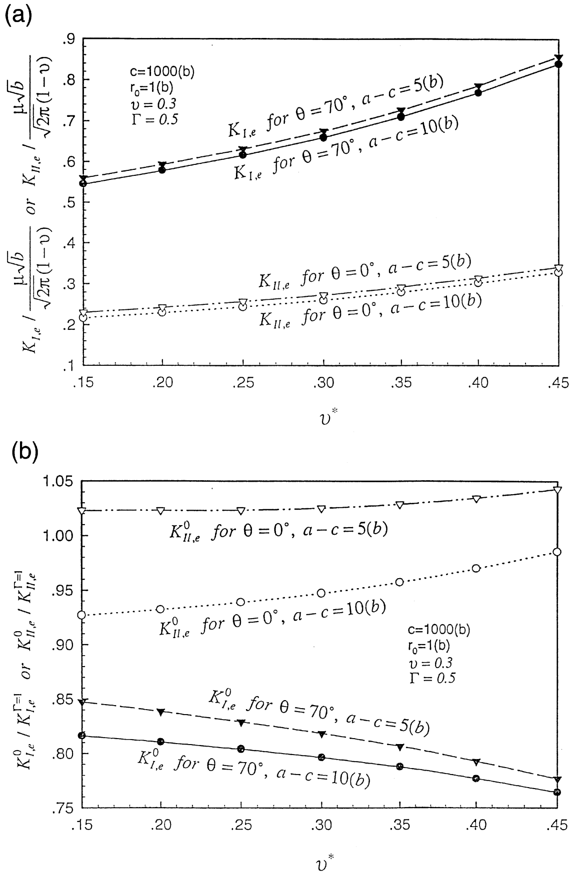

Fig. 16. (a) The critical stress intensity factors for an edge dislocation emission from the thin-film-covered crack tip as a function of the Poisson ratio of the film. (b) The nominally critical stress intensity factors for an edge dislocation emission from the thin-film-covered crack tip as a function of the Poisson ratio of the film.

used in plotting Fig. 16(a) and (b). As can be seen in Fig. 16(a) that all the critical stress intensity factors increase with increasing the Poisson ratio of the film regardless of the film thickness. However, Fig. 16(b) indicates that a large Poisson ratio of the film makes the nominally critical stress intensity factors increase for the mode II emission but decrease for the mode I emission.

4. Conclusions

Using the complex potentials, superposition, Cauchy integration, specially constructed functions, and series expansion, the present work analyses the stress fields near a thin-film-covered mode I and/or mode II crack produced by applied remote loads and an edge dislocation in the film. Focus is put on the effects of the film thickness, the shear modulus and Poisson ratio of the thin film on the stress fields, and hence the stress intensity factors. The shielding effects, the image force of an edge dislocation, and dislocation emission from the film-covered crack tip have been investigated. The following conclusions are drawn from the investigation:

1. A large ratio of shear moduli yields a high stress field and hence both large mode I and mode II stress intensity factors. This means that the stress field in front of the crack tip due to the applied loads are enhanced by a harder film or abated by a softer film.
2. A large Poisson ratio of the film enhances the stress field in the film, resulting in large stress intensity factors under the mode I or mode II loadings.
3. The slip component of the image force on an edge dislocation in the film emitted from the crack tip is proportional to the ratio of shear moduli. The image force is enhanced by a film with relatively high shear modulus and Poisson ratio in comparison with those of the substrate.
4. In conjugation with the image force, the shielding of the crack tip by an edge dislocation in the film is stronger when the film is harder, and the opposite is also true.
5. The critical stress intensity factor for dislocation emission from the crack tip is influenced by the crack length and the film stiffness as well as the film thickness. There exists a critical film thickness for a given crack length. When the film is thinner than the critical thickness, a harder film makes the dislocation emission easier, while a softer film makes the emission more difficult.

Acknowledgements

The work is supported by the Hong Kong Research Grants Council under RGC Grant, HKUST 819/96 E.

Appendix A. Sfress fields due to applied remote loads

Wu and Chen (1990) have established the solution of stress fields due to applied remote loads. In this study, we employ a slightly different approach. Using superposition, we divide the complex potentials for the film and substrate under applied-remote loadings into three parts

$$\phi^*(\zeta) = \phi_1^*(\zeta) + \phi_2^*(\zeta) + \phi_3^*(\zeta),$$

$$\psi^*(\zeta) = \psi_1^*(\zeta) + \psi_2^*(\zeta) + \psi_3^*(\zeta),$$

$$\phi(\zeta) = \phi_1(\zeta) + \phi_2(\zeta) + \phi_3(\zeta),$$

$$\psi(\zeta) = \psi_1(\zeta) + \psi_2(\zeta) + \psi_3(\zeta). \tag{A1}$$

Let the first part be the solutions for an elliptical inclusion without any crack under applied remote loads and have the following forms:

$$\phi_1^*(\zeta) = c_1 z = c_1 R(\zeta + m/\zeta), \tag{A2}$$

$$\psi_1^*(\zeta) = c_2 z = c_2 R(\zeta + m/\zeta), \tag{A3}$$

for the film; and,

$$\frac{\phi_1(\zeta)}{R} = \left[a_1c_1 + a_2(\overline{c_1} + m\overline{c_2})\right]\zeta + \frac{\left[ma_1c_1 + a_2(m\overline{c_1} + \overline{c_2})\right]}{\zeta}, \tag{A4}$$

$$\frac{\psi_1(\zeta)}{R} = \left[a_4c_2 + m\big((a_3 - a_2)\overline{c_1} + (a_4 - a_1)c_1 - ma_2\overline{c_2}\big)\right]\zeta + \frac{\left[ma_4c_2 + (a_3 - a_2)\overline{c_1} + (a_4 - a_1)c_1\right]}{\zeta} - a_2\overline{c_2}\frac{\left(m^3\zeta^2 - 1\right)}{\zeta\left(\zeta^2 - m\right)}, \tag{A5}$$

for the substrate; where c_1 and c_2 are constants that will be determined by the remote loads. The traction along the crack faces produced by the first part of the stress fields is then given by

$$T = \sigma_{22}^* - i\sigma_{12}^* = c_1 + \overline{c_1} + \overline{c_2}. \tag{A6}$$

The second part of the complex potentials for the film is formulated from the traction-free condition along the crack faces. Using Eqs. (4) and (A6), we have

$$\frac{\phi_2^*(\zeta)}{R} = -\frac{mT}{\zeta}, \tag{A7}$$

$$\frac{\psi_2^*(\zeta)}{R} = -\frac{m\bar{T}}{\zeta} - \frac{mT}{\zeta}\frac{\zeta + m/\zeta}{\zeta - m/\zeta}. \tag{A8}$$

The second parts of the complex potentials for the substrate are analytically derived from the continuity of displacement and traction along the interface by applying Cauchy integration to Eqs. (5) and (6). Using Eqs. (5), (6), (A7) and (A8), and completing the integration yield

$$\frac{\phi_2(\zeta)}{R} = -\frac{a_1mT}{\zeta} + a_2(m\bar{T} - mT - \bar{T})\zeta, \tag{A9}$$

$$\frac{\psi_2(\zeta)}{R} = -a_3m\bar{T}\zeta + \frac{1 + m\zeta^2}{\zeta^2 - m}\left[(a_4 - a_1)\frac{mT}{\zeta} - \zeta a_2(m\bar{T} - mT - \bar{T})\right] - a_4\left[\frac{m\bar{T}}{\zeta} + \frac{mT}{\zeta}\frac{\zeta^2 + m}{\zeta^2 - m}\right]. \tag{A10}$$

Note that Eqs. (A9), (A10), (A7) and (A8) cannot totally satisfy the boundary conditions of Eqs. (5) and (6), because the values of Eqs. (A7) and (A8) at the interface are not the exact boundary values of the complex potentials for the substrate. Doing this, however, analytically maximizes the solutions. The remote loading conditions require

$$(a_1 - a_2)c_1 + a_2(m - 1)c_2 = \frac{\sigma_{11}^\infty + \sigma_{22}^\infty}{4}, \tag{A11}$$

$$\left[a_4 - a_2m^2 - m(a_3 - a_2)\right]c_2 + m(a_4 - a_1 + a_2 - a_3)c_1 = \frac{\sigma_{22}^\infty - \sigma_{11}^\infty}{2} + i\sigma_{12}^\infty. \tag{A12}$$

Solving Eqs. (A11) and (A12) gives the constants c_1 and c_2:

$$c_1 = \frac{P_2}{2P_1} + i\frac{\sigma_{12}^\infty}{P_1},$$

$$c_2 = \frac{\sigma_{11}^{\infty} + \sigma_{22}^{\infty}}{4(m-1)a_2} - \frac{a_1 - a_2}{(m-1)a_2} c_1. \tag{A13}$$

where

$$P_1 = m(a_4 - a_1 + a_2 - a_3) - \frac{(a_1 - a_2)\left[a_4 - m^2 a_2 - m(a_3 - a_2)\right]}{(m-1)a_2},$$

$$P_2 = \sigma_{22}^{\infty} - \sigma_{11}^{\infty} - \frac{\left[a_4 - m^2 a_2 - m(a_3 - a_2)\right]}{(m-1)a_2} \frac{\sigma_{11}^{\infty} + \sigma_{22}^{\infty}}{2}. \tag{A14}$$

In order to satisfy the interface boundary conditions totally, the third parts of the complex potentials for the substrate and for the film are introduced and expressed by the following series:

$$\phi_3(\zeta) = \sum_{n=-\infty}^{0} A_n \zeta^n, \qquad \psi_3(\zeta) = \sum_{n=-\infty}^{0} B_n \zeta^n, \tag{A15}$$

$$\phi_3^*(\zeta) = \sum_{n=-\infty}^{\infty} C_n \zeta^n, \tag{A16}$$

where A_n, B_n and C_n are constants to be determined by the boundary conditions. Hence, it follows that no stress at infinity are induced by the third part of the complex potentials for the substrate, the index n in the series of ϕ_3 and ψ_3 has to be counted from $-\infty$ to 0. Using analytic continuation from the traction-free condition along the crack faces results in the third part of the complex potential $\psi^*(\zeta)$ for the film. It is

$$\psi_3^*(\zeta) = -\sum_{n=-\infty}^{\infty} \overline{C_n} m^n \zeta^{-n} - \frac{m/\zeta + \zeta}{1 - m/\zeta^2} \sum_{n=-\infty}^{\infty} C_n n \zeta^{n-1}. \tag{A17}$$

Since the second part cannot totally satisfy the boundary conditions along the interface, both the second and the third part are used to meet the boundary conditions. From the continuity of displacement and traction along the interface, we have

$$\begin{aligned} \sum_{n=-\infty}^{0} A_n \mathrm{e}^{in\theta} = {} & \sum_{n=-\infty}^{\infty} (a_1 - a_2 m^n) C_n \mathrm{e}^{in\theta} + a_2(m-1) \frac{\mathrm{e}^{-i\theta} - \mathrm{e}^{i\theta}}{1 - m\mathrm{e}^{i2\theta}} \sum_{n=-\infty}^{\infty} \overline{C_n} n \mathrm{e}^{i(1-n)\theta} \\ & + a_2 R \frac{1 - 2m + m^2}{1 - m\mathrm{e}^{i2\theta}} \bar{T} \mathrm{e}^{i\theta}, \end{aligned} \tag{A18}$$

and

$$\begin{aligned} & \frac{\mathrm{e}^{i\theta} + m\mathrm{e}^{-i\theta}}{1 - m\mathrm{e}^{i2\theta}} \sum_{n=-\infty}^{0} \overline{A_n} n \mathrm{e}^{i(1-n)\theta} + \sum_{n=-\infty}^{0} \overline{B_n} \mathrm{e}^{-in\theta} \\ & = a_3 \sum_{n=-\infty}^{\infty} C_n \mathrm{e}^{in\theta} + a_4(m-1) \frac{\mathrm{e}^{-i\theta} - \mathrm{e}^{i\theta}}{1 - m\mathrm{e}^{i2\theta}} \sum_{n=-\infty}^{\infty} \overline{C_n} n \mathrm{e}^{i(1-n)\theta} - a_4 \sum_{n=-\infty}^{\infty} C_n m^n \mathrm{e}^{in\theta}. \end{aligned} \tag{A19}$$

Eqs. (A18) and (A19) have to be numerically solved to evaluate constants A_n, B_n and C_n.

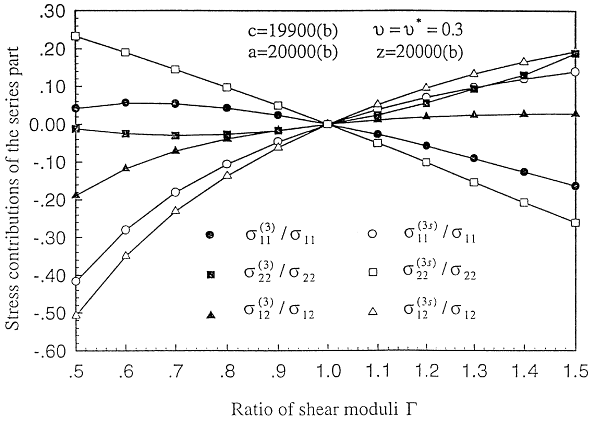

Fig. A1. Stress contributions of the series parts with or without the Cauchy integration.

The purpose of conducting the above mentioned Cauchy integration is to achieve the analytical solution of the complex potentials for the substrate as much as possible. Thus, the third parts, which actually take finite terms for each series in the numerical evaluation, will make the smallest contributions to the solution. To demonstrate this phenomena, stresses at the interface are calculated for $c = 19{,}900b$ and $a = 20{,}000b$ under the assumption that both the film and the substrate have the same Poisson ratio of 0.3. Fig. A1 shows the contribution from the series to the stresses with or without conducting the Cauchy integration, where $\sigma_{11}^{(3)}$, $\sigma_{22}^{(3)}$ and $\sigma_{12}^{(3)}$ are calculated using the above combined Cauchy integration and the series expansion technique, and $\sigma_{11}^{(3s)}$, $\sigma_{22}^{(3s)}$ and $\sigma_{12}^{(3s)}$ are calculated without conducting the Cauchy integration and assuming that $\Phi_2(\zeta)$ and $\Psi_2(\zeta)$ are the same as $\phi_2^*(\zeta)$ and $\Psi_2^*(\zeta)$. As expected, no contributions come from the series when the film and the substrate are identical, i.e., the ratio of shear moduli Γ equals unity, as shown in Fig. A1. For $\Gamma = 1.5$, the stress contributions of the series parts without conducting the Cauchy integration are, respectively, $|\sigma_{11}^{(3s)}/\sigma_{11}| = 15\%$, $|\sigma_{22}^{(3s)}/\sigma_{22}| = 25\%$ and $|\sigma_{12}^{(3s)}/\sigma_{12}| = 20\%$, while conducting the Cauchy integration reduced the corresponding stress contributions of the series parts to 15%, 20% and 5%, respectively. The reduction is larger if the film is softer than the substrate. Take $\Gamma = 0.5$ for an example. The stress contributions of the series parts without conducting the Cauchy integration are, respectively, $|\sigma_{11}^{(3s)}/\sigma_{11}| = 42\%$, $|\sigma_{22}^{(3s)}/\sigma_{22}| = 24\%$ and $|\sigma_{12}^{(3s)}/\sigma_{12}| = 52\%$, while the corresponding stress contributions of the series parts with conducting the Cauchy integration are 4%, 2% and 20%, respectively. It is clear that applying the Cauchy integration before numerical evaluation reduces the contribution of the series and therefore simplifies the numerical computation.

Appendix B. Stress fields due to an edge dislocation in the film

Using the same approach as used for the remote applied loads, we divide the complex potentials for the film into three parts and the complex potentials for the substrate into two parts. The first parts of the complex potentials for the film are given below as the solution for an edge dislocation near a finite length crack inside a homogeneous medium (Zhang and Li, 1991).

$$\phi_1^*(\zeta) = \gamma\ln(\zeta - \zeta_d) - \gamma\ln\left(\zeta - \frac{m}{\overline{\zeta_d}}\right) - \frac{\bar{\gamma} m(z_d - \overline{z_d})/R}{\overline{\zeta_d}\left(\overline{\zeta_d} - m/\overline{\zeta_d}\right)\left(\zeta - m/\overline{\zeta_d}\right)} + C, \tag{B1}$$

$$\psi_1^*(\zeta) = \bar{\gamma}\ln(\zeta - \zeta_{\rm d}) - \bar{\gamma}\ln\left(\zeta - \frac{m}{\overline{\zeta_{\rm d}}}\right) - \frac{\gamma\zeta_{\rm d}(\overline{z_{\rm d}} - z_{\rm d})/R}{(\zeta_{\rm d} - m/\zeta_{\rm d})(\zeta - \zeta_{\rm d})} - \frac{m/\zeta + \zeta}{1 - m/\zeta^2}\left[\frac{\gamma}{\zeta - \zeta_{\rm d}} - \frac{\gamma}{\zeta - m/\overline{\zeta_{\rm d}}} + \frac{\bar{\gamma}m(z_{\rm d} - \overline{z_{\rm d}})/R}{\overline{\zeta_{\rm d}}\left(\overline{\zeta_{\rm d}} - m/\overline{\zeta_{\rm d}}\right)\left(\zeta - m/\overline{\zeta_{\rm d}}\right)^2}\right] + C, \tag{B2}$$

where $\gamma = [\mu(b_1 + ib_2)]/[i4\pi(1 - \nu)]$, and C is a constant that does not make any contributions to the stress fields. Applying Cauchy integration to Eqs. (8) and (9), we have

$$\begin{aligned}&\frac{1}{2\pi i}\oint[\phi_1(t) + \phi_2(t)]\,\frac{{\rm d}t}{t - \zeta}\\ &= \frac{a_1}{2\pi i}\oint[\phi_1^*(t) + \phi_2^*(t) + \phi_3^*(t)]\,\frac{{\rm d}t}{t - \zeta} + \frac{a_2}{2\pi i}\oint\left\{\frac{t + m/t}{1 - mt^2}\left[\overline{\phi_1^{*\prime}}\left(\frac{1}{t}\right) + \overline{\phi_2^{*\prime}}\left(\frac{1}{t}\right) + \overline{\phi_3^{*\prime}}\left(\frac{1}{t}\right)\right]\right.\\ &\quad\left. + \overline{\psi_1^*}\left(\frac{1}{t}\right) + \overline{\psi_2^*}\left(\frac{1}{t}\right) + \overline{\psi_3^*}\left(\frac{1}{t}\right)\right\}\,\frac{{\rm d}t}{t - \zeta},\end{aligned} \tag{B3}$$

$$\begin{aligned}&\frac{1}{2\pi i}\oint\left\{\frac{1/t + mt}{1 - m/t^2}[\phi_1'(t) + \phi_2'(t)]\right\}\,\frac{{\rm d}t}{t - \zeta} + \frac{1}{2\pi i}\oint[\psi_1(t) + \psi_2(t)]\,\frac{{\rm d}t}{t - \zeta}\\ &= \frac{a_3}{2\pi i}\oint\left[\overline{\phi_1^*}\left(\frac{1}{t}\right) + \overline{\phi_2^*}\left(\frac{1}{t}\right) + \overline{\phi_3^*}\left(\frac{1}{t}\right)\right]\,\frac{{\rm d}t}{t - \zeta} + \frac{a_4}{2\pi i}\oint\left\{\frac{1/t + mt}{1 - m/t^2}[\phi_1^{*\prime}(t) + \phi_2^{*\prime}(t) + \phi_3^{*\prime}(t)]\right.\\ &\quad\left. + \psi_1^*(t) + \psi_2^*(t) + \psi_3^*(t)\right\}\,\frac{{\rm d}t}{t - \zeta}.\end{aligned} \tag{B4}$$

In Eq. (B3), the integrand involving $\overline{\psi_1^*}(\frac{1}{\zeta})$ contains a logarithmic term $\overline{\psi_0^*}(\frac{1}{\zeta}) = \gamma\ln\frac{\zeta - 1/\overline{\zeta_{\rm d}}}{\zeta - \zeta_{\rm d}/m}$ which is singular in the substrate. We construct $\phi_{2p}^{*(1)}(\zeta) = -\frac{a_2}{a_1}\overline{\psi_0^*}(\frac{1}{\zeta})$ to cancel these terms, but from the traction-free condition along the crack surface another logarithm term $\psi_{2p}^{*(1)}(\zeta) \propto -\overline{\phi_{2p}^*}(\frac{m}{\zeta})$ will concur and $\psi_{2p}^{*(1)}(\frac{1}{\zeta})$ is also singular in the substrate. Again, we construct $\phi_{2p}^{*(2)}(\zeta) = -\frac{a_2}{a_1}\psi_{2p}^{*(1)}(\frac{1}{\zeta})$ to cancel $\psi_{2p}^{*(1)}(\frac{1}{\zeta})$ and so on. Thus, we have

$$\phi_{2p}^*(\zeta) = \sum_{n=1}^{\infty}(-1)^{n-1}G_1^n\gamma\ln\frac{\zeta - 1/\left(m^{n-1}\overline{\zeta_{\rm d}}\right)}{\zeta - \zeta_{\rm d}/m^n}, \tag{B5}$$

$$\psi_{2p}^*(\zeta) = \sum_{n=1}^{\infty}(-1)^n G_1^n\bar{\gamma}\ln\frac{\zeta - m^n\zeta_{\rm d}}{\zeta - m^{n+1}/\overline{\zeta_{\rm d}}}, \tag{B6}$$

where $G_1 = -a_2/a_1$ and the absolute value of G_1 is always less than unity. It is seen that $\psi_{2p}^*(\zeta)$ and $\phi_{2p}^*(\zeta)$ are convergent and analytic in the substrate.

Similarly, $\overline{\phi_1^*}(\frac{1}{\zeta})$ in Eq. (B4) contains a singular logarithm term $\overline{\phi_0^*}(\frac{1}{\zeta}) = \bar{\gamma}\ln\frac{\zeta - 1/\overline{\zeta_{\rm d}}}{\zeta - \zeta_{\rm d}/m}$, so we construct $\psi_{2s}^{*(1)}(\zeta) = -\frac{a_3}{a_4}\overline{\phi_0^*}(\frac{1}{\zeta})$ to cancel it. In order to cancel the singular logarithm term $\overline{\phi_{2s}^{*(1)}}(\frac{1}{\zeta})$ that occurred due to the requirement of traction-free along crack surface, $\psi_{2s}^{*(2)}(\zeta)$ is needed and so on. Thus, we have

$$\phi^*_{2s}(\zeta) = \sum_{n=1}^{\infty} (-1)^n G_2^n \gamma \ln \frac{\zeta - m^n \zeta_{\mathrm{d}}}{\zeta - m^{n+1}/\overline{\zeta}_{\mathrm{d}}}, \tag{B7}$$

$$\psi^*_{2s}(\zeta) = \sum_{n=1}^{\infty} (-1)^{n-1} G_2^n \overline{\gamma} \ln \frac{\zeta - 1/\left(m^{n-1}\overline{\zeta}_{\mathrm{d}}\right)}{\zeta - \zeta_{\mathrm{d}}/m^n}, \tag{B8}$$

where $G_2 = -a_3/a_4$ and the absolute value of G_2 is less than unit when $\Gamma > 0.222$. It is seen that $\phi^*_{2s}(\zeta)$ and $\overline{\psi^*_{2s}(\zeta)}$ are convergent and analytic in the substrate. Therefore, the second parts of the complex potentials for the film are obtained as

$$\phi^*_2(\zeta) = \phi^*_{2p}(\zeta) + \phi^*_{2s}(\zeta), \tag{B9}$$

$$\psi^*_2(\zeta) = \psi^*_{2p}(\zeta) + \psi^*_{2s}(\zeta). \tag{B10}$$

The third part of the complex potential $\phi^*(\zeta)$ for the film is expressed as

$$\phi^*_3(\zeta) = \sum_{n=-\infty}^{\infty} H_n \zeta^n. \tag{B11}$$

The third part of the complex potential $\psi^*(\zeta)$ for the film is obtained from the traction-free condition along the crack surface and given by

$$\psi^*_3(\zeta) = -\sum_{n=-\infty}^{\infty} \overline{H}_n m^n \zeta^{-n} - \frac{m/\zeta + \zeta}{1 - m/\zeta^2} \phi^{*\prime}_2(\zeta) - \frac{m/\zeta + \zeta}{1 - m/\zeta^2} \sum_{n=-\infty}^{\infty} H_n n \zeta^{n-1}. \tag{B12}$$

After defining all the terms on the right sides of Eqs. (B3) and (B4), we complete the integration and substitute all the analytic and non-zero parts go into $\phi_1(\zeta)$ or $\psi_1(\zeta)$, which are finally expressed, respectively, as

$$\phi_1(\zeta) = a_1\left[\phi^*_1(\zeta) + \phi^*_{2s}(\zeta)\right] + a_2 \overline{\psi^*_{2s}(\zeta)}, \tag{B13}$$

$$\psi_1(\zeta) = -\frac{\zeta + m\zeta^3}{\zeta^2 - m} \phi_1'(\zeta) + a_3 \overline{\phi^*_{2p}(\zeta)} + a_4 \left[\frac{\zeta + m\zeta^3}{\zeta^2 - m} \phi^{*\prime}_1(\zeta) + \psi^*_1(\zeta) + \psi^*_{2p}(\zeta) \right]. \tag{B14}$$

The second parts of the complex potentials for the substrate may have the form:

$$\phi_3(\zeta) = \sum_{n=-\infty}^{0} E_n \zeta^n, \qquad \psi_3(\zeta) = \sum_{n=-\infty}^{0} F_n \zeta^n. \tag{B15}$$

The rest terms in Eqs. (B3) and (B4) constitute the following equations:

$$\begin{aligned}\sum_{n=-\infty}^{0} E_n \mathrm{e}^{in\theta} = {} & a_1 \sum_{n=-\infty}^{\infty} H_n \mathrm{e}^{in\theta} + a_2 \left\{ \frac{\mathrm{e}^{i\theta} + m\mathrm{e}^{-i\theta}}{1 - m\mathrm{e}^{i2\theta}} \left[\overline{\phi_1^{*\prime}(\mathrm{e}^{i\theta})} + \overline{\phi_2^{*\prime}(e^{i\theta})} + \sum_{n=-\infty}^{\infty} \overline{H_n} n \mathrm{e}^{i(1-n)\theta} \right] \right. \\ & + \overline{\psi_1^{*}(\mathrm{e}^{i\theta})} - \sum_{n=-\infty}^{\infty} H_n m^n \mathrm{e}^{in\theta} - \frac{m\mathrm{e}^{i\theta} + \mathrm{e}^{-i\theta}}{1 - m\mathrm{e}^{i2\theta}} \overline{\phi_2^{*\prime}(\mathrm{e}^{i\theta})} \\ & \left. - \frac{m\mathrm{e}^{i\theta} + \mathrm{e}^{-i\theta}}{1 - m\mathrm{e}^{i2\theta}} \sum_{n=-\infty}^{\infty} \overline{H_n} n \mathrm{e}^{i(1-n)\theta} \right\}, \end{aligned} \tag{B16}$$

$$\begin{aligned} & \frac{\mathrm{e}^{i\theta} + m\mathrm{e}^{-i\theta}}{1 - m\mathrm{e}^{i2\theta}} \sum_{n=-\infty}^{0} \overline{E_n} n e^{i(1-n)\theta} + \sum_{n=-\infty}^{0} \overline{F_n} \mathrm{e}^{-in\theta} \\ & = a_3 \frac{\bar{\gamma}(z_{\mathrm{d}} - \overline{z_{\mathrm{d}}})/R}{\overline{\zeta_{\mathrm{d}}} - m/\overline{\zeta_{\mathrm{d}}}} \frac{\mathrm{e}^{-i\theta}}{\mathrm{e}^{-i\theta} - \overline{\zeta_{\mathrm{d}}}/m} + \sum_{n=-\infty}^{\infty} H_n (a_3 - a_4 m^n) \mathrm{e}^{in\theta} \\ & \quad + a_4 \left\{ \frac{(1-m)\mathrm{e}^{i\theta} + (m-1)\mathrm{e}^{-i\theta}}{1 - m\mathrm{e}^{i2\theta}} \left[\overline{\phi_2^{*\prime}(\mathrm{e}^{i\theta})} + \sum_{n=-\infty}^{\infty} \overline{H_n} n \mathrm{e}^{i(1-n)\theta} \right] \right\}. \end{aligned} \tag{B17}$$

Solving Eqs. (B16) and (B17) gives the constants, E_n, F_n and H_n.

From Eq. (11), the stress intensity factors induced by an edge dislocation in the film can be formulated as

$$\begin{aligned} K_{\mathrm{I}} + iK_{\mathrm{II}} = {} & \sqrt{\frac{\pi}{2R}} m^{\frac{1}{4}} \left\{ \frac{\bar{\gamma}}{\sqrt{m} - \overline{\zeta_{\mathrm{d}}}} - \frac{\bar{\gamma}}{\sqrt{m}\left(1 - \sqrt{m}/\zeta_{\mathrm{d}}\right)} + \frac{\gamma(\overline{z_{\mathrm{d}}} - z_{\mathrm{d}})/R}{\zeta_{\mathrm{d}}(\zeta_{\mathrm{d}} - m/\zeta_{\mathrm{d}})\left(1 - \sqrt{m}/\zeta_{\mathrm{d}}\right)^2} \right. \\ & + \frac{\bar{\gamma}}{\sqrt{m} - \zeta_{\mathrm{d}}} - \frac{\bar{\gamma}}{\sqrt{m}\left(1 - \sqrt{m}/\overline{\zeta_d}\right)} + \frac{\gamma \xi_{\mathrm{d}}(\overline{z_{\mathrm{d}}} - z_d)/R}{(\zeta_{\mathrm{d}} - m/\zeta_{\mathrm{d}})\left(\sqrt{m} - \zeta_d\right)^2} \\ & + \sum_{n=1}^{\infty} (-1)^{n-1} G_1^n \bar{\gamma} \left[\frac{1}{\sqrt{m} - 1/\left(m^{n-1}\zeta_{\mathrm{d}}\right)} - \frac{1}{\sqrt{m} - \overline{\zeta_{\mathrm{d}}}/m^n} \right] \\ & + \sum_{n=1}^{\infty} (-1)^{n} G_2^n \bar{\gamma} \left(\frac{1}{\sqrt{m} - m^n \overline{\zeta_{\mathrm{d}}}} - \frac{1}{\sqrt{m} - m^{n+1}/\zeta_{\mathrm{d}}} \right) \\ & + \sum_{n=1}^{\infty} (-1)^{n} G_1^n \bar{\gamma} \left(\frac{1}{\sqrt{m} - m^n \zeta_{\mathrm{d}}} - \frac{1}{\sqrt{m} - m^{n+1}/\overline{\zeta_{\mathrm{d}}}} \right) \\ & \left. + \sum_{n=1}^{\infty} (-1)^{n-1} G_2^n \bar{\gamma} \left[\frac{1}{\sqrt{m} - 1/\left(m^{n-1}\overline{\zeta_{\mathrm{d}}}\right)} - \frac{1}{\sqrt{m} - \zeta_{\mathrm{d}}/m^n} \right] + 2 \sum_{n=-\infty}^{\infty} \overline{H_n} n m^{\frac{n-1}{2}} \right\}. \end{aligned} \tag{B18}$$

It should be pointed out that constructing $\phi_2^*(\zeta)$ and $\psi_2^*(\zeta)$ to cancel the singular (in the infinite medium) logarithm terms can greatly facilitate the numerical evaluation of the constants E_n, F_n, and H_n. Otherwise, derivative operations were applied on every term of Eqs. (B16) and (B17), which would make the numerical calculation of the constants, E_n, F_n, and H_n, much more difficult or even impossible. It turns out numerically that the series in (Eqs. (B5)–(B8)) converge so fast that 10 terms are enough for $\phi_2^*(\zeta)$ and $\psi_2^*(\zeta)$ because both absolute values of G_1 and G_2 in $\phi_2^*(\zeta)$ and $\psi_2^*(\zeta)$ are smaller than unity.

Appendix C. Effects of the film thickness on the screw dislocation emission from a thin-film-covered mode III crack

For a mode III thin-film-covered crack embedded, the stress intensity factor due to the applied load, σ_{32}^{∞}, is given by (Zhang and Qian, 1996a)

$$K_{\text{III}} = \frac{2\Gamma}{1+\Gamma+m(1-\Gamma)} K_{\text{III}}^{0} \tag{C1}$$

where $K_{\text{III}}^{0} = \sigma_{32}^{\infty}\sqrt{\pi c}$. When the film thickness is much smaller than the half-crack length, (C1) can be reduced to

$$K_{\text{III}} = \Gamma K_{\text{III}}^{0}. \tag{C2}$$

The error, ER, using the approximate equation of (C2) can be evaluated by

$$ER = \left| \frac{\dfrac{2\Gamma}{1+\Gamma+m(1-\Gamma)} K_{\text{III}}^{0} - \Gamma K_{\text{III}}^{0}}{\dfrac{2\Gamma}{1+\Gamma+m(1-\Gamma)} K_{\text{III}}^{0}} \right| = \frac{1}{2}(1-m)|1-\Gamma|. \tag{C3}$$

Eq. (C3) indicates that the error is small if the parameter, m, is close to unity. A soft film makes the ratio of shear moduli small and then the error small, while a hard film may increase the error. For the range 0.1–10 of the ratio of shear moduli, a 5% error requires the film thickness to be five order smaller than the crack length.

Based on the Rice–Thomson model (Rice and Thomson, 1974), the nominally critical stress intensity factor (NCSIF) for dislocation emission is given by

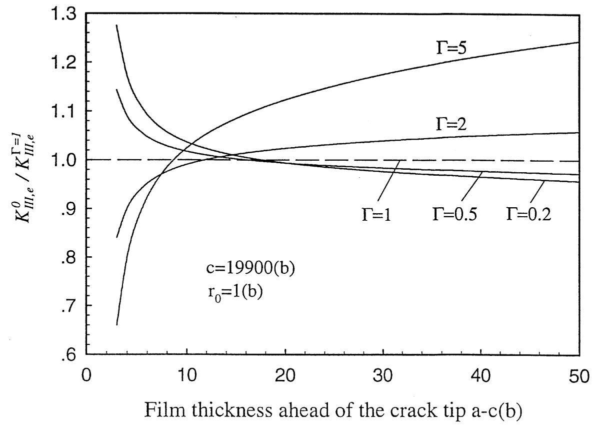

Fig. C1. The normalized nominally critical stress intensity factor as a function of the filmthickness for different shear modulus ratios.

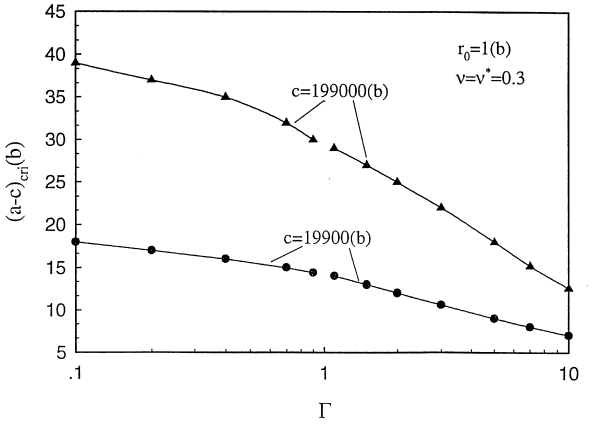

Fig. C2. The critical thickness as a function of the shear modulus ratio for the crack lengths of $c = 19{,}900b$ and $c = 199{,}000b$.

$$K^0_{\mathrm{III,\,e}} = \frac{[1+\Gamma+m(1-\Gamma)]\mu b}{4\sqrt{\pi}}\left\{\frac{1}{\sqrt{2r_0}} - \frac{(\Gamma-1)\sqrt{c}}{2R} \times \sum_{n=1}^{\infty}\left[\left(\frac{c+\sqrt{2cr_0}}{2R}\right)^{2n} - \left(\frac{2Rm}{c+\sqrt{2cr_0}}\right)^{2n}\right]\frac{1}{\Gamma(1-m^n)+1+m^n}\right\}, \tag{C4}$$

where b denotes the Burgers vector of the screw dislocation and remains the meaning hereafter in Appendix C and in Figs. C1 and C2. Fig. C1 illustrates the variation of the normalized NCSIFs with the film thickness for $\Gamma = 0.2$, 0.5, 2.0 and 5.0. When the normalized NCSIF equals to unity, the film has no influence on the dislocation emission. For a small film thickness, e.g. $a–c = 5b$, as can be seen in Fig. C1, the larger the shear modulus ratio (i.e. the harder the film), the smaller the NCSIF. This means that a harder film makes the dislocation emission easier when the film thickness is small, while a soft film makes it more difficult. For a large film thickness, e.g. $a–c = 50b$, however, the conclusion is just opposite to that for a small thickness. There exists a critical film thickness at which the normalized NCSIF equals one. When the film thickness is less than the critical one, the dislocation emission is easier for a hard film ($\Gamma > 1$), but more difficult for a soft film ($\Gamma < 1$). The opposite is also true when the film thickness is larger than the critical one. Fig. C2 shows the critical film thickness as a function of the shear modulus ratio for the half-crack lengths of $c = 19{,}900b$ and $c = 199{,}000b$. When $\Gamma = 1$, there is no solution for the critical thickness. As can be seen in Fig. C2, the critical thickness decreases with increasing and the critical thickness for $c = 199{,}000b$ is much larger than that for $c = 19{,}900b$ at a given shear modulus ratio. This means that if the film is softer than the substrate and the crack is longer, the critical thickness will be larger.

References

Anlas, G., Santare, M.H., 1993. Arbitrarily oriented crack inside an elliptical inclusion. J. App. Mech., ASME 60, 589–594.

Asaro, R.J., 1975. An image force theorem for a dislocation near a crack in an anisotropic elastic medium. J. Phys. F., Metal Phys 5, 2249–2255.

Chen, D.H., 1995. A point force and an edge dislocation in an elliptical inclusion embedded in an infinite medium. Int. J. Fract 71, 311–322.

Chen, W.T., 1967. On an elliptic elastic inclusion in an anisotropic medium. Q. J. Mech. App. Math 20, 307–313.

Dundurs, J., Mura, T., 1964. Interaction between an edge dislocation and a circular inclusion. J. Mech. Phys. Solids 12, 177–189.

Dundurs, J., Sendeckyj, G.P., 1965. Edge dislocation inside a circular inclusion. J. Mech. Phys. Solids 13, 141–147.

Erdogan, F., Gupta, G.D., Ratwani, M., 1974. Interaction between a circle inclusion and an arbitrarily oriented crack. J. App. Mech. ASME 41, 1007–1013.

Eshelby, J.D., 1957. The determination of the elastic field of an ellipsoidal inclusion, and related problems. Proc. Roy. Soc. A241, 376–396.

Flanagan, W.F., Zhong, L., Lichter, B.D., 1993. A mechanism for transgranular stresscorrosion cracking. Metall. Trans. A 24A, 553–559.

Gong, S.X., 1994. Antiplane interaction of line crack with an arbitrarily located elliptical inclusion. Theore. App. Fract. Mech 20, 193–205.

Honein, T.E., Herrmann, G., 1994. Circularly cylindrical and plane layered media in antiplane elastostatics. J. App. Mech., ASME 61, 243–249.

Jones, R.H., Ricker, R.E., 1992. Mechanisms of stress-corrosion cracking. In: Jones, R.H. (Ed.), Stress Corrosion Cracking. ASM International, pp. 1–40.

Kaufman, M.J., Fink, J.L., 1988. Evidence for localized ductile fracture in the "brittle" transgranular stress corrosion cracking of ductile F.C.C. alloys. Acta Metall 36, 2213–2228.

Lin, I.H., Thomson, R., 1986. Cleavage, dislocation emission, and shielding for cracks under general loading. Acta Metall 34, 187–206.

Magnin, Th., 1996. Advances in Corrosion–Deformation Interactions. Trans Tech Publications, Lebanon, USA.

Mura, T., 1982. Micromechanics of Defects in Solids. Martinus Nijhoff, Dordrecht, Boston.

Mura, T., 1988. Inclusion problems. Appl. Mech. Review, ASME, New York 41, 15–20.

Muskhelishvili, N., 1954. Some basic problems of the mathematical theory of elasticity. Moscow, Russia.

Parkins, R.N., 1992. Current understanding of stress-corrosion cracking. JOM 44, 12–19.

Patton, E.M., Santare, M.H., 1990. The effect of rigid elliptical inclusion on a straight crack. Int. J. Fract 46, 71–79.

Qaissaunee, M., 1992. Elastic elliptical inclusion and dislocation interaction problems. M.S. Thesis, University of Delaware, Newark, DE.

Qaissaunee, M.T., Santare, M.H., 1995. Edge dislocation interacting with an elliptical inclusion surrounded by an interfacial zone. Q. J. Mech. App. Math 48, 465–482.

Qian, Cai-Fu, Li, J.C.M., 1996a. Edge dislocations emitted along multiple inclined slip planes from a mode I crack. Part I: Sequential emission. Mech. Mater 24, 1–10.

Qian, Cai-Fu., Li, J.C.M., 1996b. Edge dislocations emitted along multiple inclined slip planes from a mode I crack. Part II: Simultaneous emission. Mech. Mater 24, 11–17.

Rice, J.R., Thomson, R., 1974. Ductile versus brittle behavior of crystals. Phil. Mag 29, 73–97.

Santare, M.H., 1995. Dislocation inside an isotropic elliptical inclusion surrounded by an anisotropic medium. J. App. Mech., ASME 62, 537–539.

Santare, M.H., Keer, L.M., 1986. Interaction between an edge dislocation and a rigid elliptical inclusion. J. App. Mech., ASME 53, 382–385.

Sieradzki, K., 1982. The effect of thin film formation at crack tips on fracture. Acta Metall 30, 973–982.

Sieradzki, K., Newman, R.C., 1985. Brittle behavior of ductile metals during stress-corrosion cracking. Phil. Mag A51, 95–132.

Sieradzki, K., Newman, R.C., 1987. J. Phys. Chem. Solids 48, 1101–1113.

Stagni, L., Lizzio, R., 1983. Shape effects in the interaction between an edge dislocation and an elliptic inclusion. J. App. Phys A30, 217–221.

Tong, Pin, Zhang, Tong-Yi., 1996. A dislocation in a nearly polygonal isotropic domain. Int. J. Fract 78, 241–260.

Warren, W.E., 1983. The edge dislocation inside an elliptical inclusion. Mech. Mater 2, 319–330.

Wu, C.H., Chen, C.H., 1990. A crack in a confocal elliptical inhomogeneity embedded in an infinite medium. J. App. Mech., ASME 57, 91–96.

Yang, H.C., Chou, Y.T., 1976. Generalized plane problems of elastic inclusions in anisotropic solids. J. App. Mech. ASME 98, 424–430.

Yen, W.J., Hwu, C., 1994. Interaction between dislocations and anisotropic elliptical inclusions. J App. Mech., ASME 61, 548–554.

Yen, W.J., Hwu, C., Liang, Y.K., 1995. Dislocation inside, outside, or on the interface of an anisotropic elliptical inclusion. J. App. Mech 62, 306–311.

Zhang, Tong-Yi., Li, J.C.M., 1991. Image forces and shielding effects of an edge dislocation near a finite length crack. Acta Metall. Mater 39, 2739–2744.

Zhang, Tong-Yi., Qian, Cai-Fu., 1996a. Interaction of a screw dislocation with a thin-filmcovered mode III crack. Acta Mater 44, 4513–4520.

Zhang, Tong-Yi., Qian, Cai-Fu, 1996b. Interaction of a thin-film-covered mode III crack with screw dislocations: emission of a screw dislocation dipole from the interface. Mech. Mater 24, 159–173.